

Northumbria Research Link

Citation: Ren, Bingzhi, Lu, Jianwei, Wang, Yucheng, Gu, Xingxing, Xu, Bin, Fu, Richard, Luo, Kun, Bayati, Maryam and Liu, Xiaoteng (2020) Half-Sphere Shell Supported Pt Catalyst for Electrochemical Methanol Oxidation. *Journal of the Electrochemical Society*, 167 (8). 084510. ISSN 0013-4651

Published by: Electrochemical Society

URL: <https://doi.org/10.1149/1945-7111/ab8dde> <<https://doi.org/10.1149/1945-7111/ab8dde>>

This version was downloaded from Northumbria Research Link:
<http://nrl.northumbria.ac.uk/id/eprint/42972/>

Northumbria University has developed Northumbria Research Link (NRL) to enable users to access the University's research output. Copyright © and moral rights for items on NRL are retained by the individual author(s) and/or other copyright owners. Single copies of full items can be reproduced, displayed or performed, and given to third parties in any format or medium for personal research or study, educational, or not-for-profit purposes without prior permission or charge, provided the authors, title and full bibliographic details are given, as well as a hyperlink and/or URL to the original metadata page. The content must not be changed in any way. Full items must not be sold commercially in any format or medium without formal permission of the copyright holder. The full policy is available online: <http://nrl.northumbria.ac.uk/policies.html>

This document may differ from the final, published version of the research and has been made available online in accordance with publisher policies. To read and/or cite from the published version of the research, please visit the publisher's website (a subscription may be required.)

Half-Sphere Shell Supported Pt Catalyst for Electrochemical Methanol Oxidation

Bingzhi Ren^{a,1}, Jianwei Lu^{b,2}, Yucheng Wang^b, Xingxing Gu^b, Ben Bin Xu^b,
Yongqing Fu^b, Kun Luo^c, Maryam Bayati^{d,*} and Terence Xiaoteng Liu^{b,*}

^a School of Metallurgical and Materials Engineering, Chongqing University of Science & Technology, Chongqing 401331, China

^b Faculty of Engineering and Environment, Northumbria University, Newcastle upon Tyne, NE1 8ST, U.K.

^c School of Materials Science and Engineering, Changzhou University, Changzhou, P. R. China, 213164

^d Department of Engineering and Mathematics, Sheffield Hallam University, Sheffield, S11WB, U.K.

***Corresponding author:**

Email: terence.liu@northumbria.ac.uk; M.Bayati@shu.ac.uk

¹ and ², these authors contributed equally to this work

Abstract:

Bi-functional effect, elevated mass transport and increased durability have been combined within one catalyst for electrochemical methanol oxidation reaction. It has niobium (Nb) doped titanium dioxides (TiO₂) nanosized half-sphere shell (HSS) as the substrate material deposited with small amount of Pt nanoparticles. These specially designed HSS nanostructure has significantly increased surface areas which are suitable for Pt nanoparticles to be deposited onto them to form the catalyst denoted as Pt/Nb-TiO₂ HSS. It exhibits a remarkably high methanol oxidation activity of 0.21 V vs. RHE which is 0.05 V lower than HiSPEC10000 PtRu/C catalyst, due to the substrate's **strong metal support interactions effect**, bi-functional effect **and the special structure**. These HSS nanostructures have also increased the methanol diffusion and mass transport within the anode to give a maximum power output of 0.0931 W of cathode polarization in miniature direct methanol fuel cell (DMFC). It also acts as protection shells, which minimises the dissolution of Pt metal nanoparticles to prevent its diffusion through the membrane.

Keywords:

Electrochemical methanol oxidation, half-sphere shell, catalytic activity, durability, mass transport

1. Introduction

Activity and durability of electrochemical methanol oxidation catalysts directly affect the performance of direct methanol fuel cells (DMFCs). This type fuel cell has been considered as one of the most promising portable power sources due to their high energy density and rapid refuelling capability⁽¹⁻⁴⁾. However, the high cost, poor durability of catalysts, and other critical issues such as noble metal dissolution and methanol crossover, **making** them less competitive than **Li rechargeable** batteries. Currently Pt-based electro-catalysts for methanol electro-oxidation have been widely investigated as the anode catalysts for DMFCs. However, there is often a de-activation problem of the Pt based catalysts which is mainly caused by the formation of strong Pt=CO bonds during, thus it will leave insufficient **active** surface to form hydroxyl groups which react with CO_{ad} via the Langmuir-Hinshelwood mechanism⁽⁵⁾. To overcome this issue, another metal element, e.g. Ru⁽⁶⁾, Sn⁽⁷⁾, Pd^(8,9) or Ni^(7,10) *etc.*, is normally introduced into the catalyst to provide hydroxyl groups according to bi-functional mechanism. This second metal has to be located adjacent to Pt in order to efficiently provide hydroxyl groups which will react with Pt=CO to produce CO₂. These can be achieved through alloying^(11,12) or formation of special nanostructures, e.g. core-shell⁽¹³⁻¹⁵⁾, nanoframe or nanowires^(15,16) *etc.* However, there are still various drawbacks. For example, highly porous carbon supported PtRu catalyst is now commercially available, and Ru is introduced as a bi-functional element to provide hydroxides to facilitate the reactions and prevent poisoning effect of the catalyst, however, it was reported that Ru (and small amount of Pt) dissolution^(17,18) and its cross-over through the membrane which dramatically **affects** the performance of the DMFCs.

Metal-oxide nanomaterials have recently attracted significant attention in different applications such as photocatalysis⁽¹⁹⁻²²⁾, solar energy conversion⁽²³⁻²⁶⁾, gas sensing^(27,28), and fuel cell

catalysts ^(3, 29, 30). Among various metal-oxide materials, TiO₂ has been regarded as the most prominent one due to its unique electrochemical and physical properties, as well as good chemical stability and low cost ⁽³¹⁾. In recent years, modified TiO₂ nanoparticles have also been applied as advanced materials for fuel cell catalyst substrates. In terms of its applications in DMFCs, Nb doped TiO₂ nanoparticles which contain both TiO_x and NbO_x have been confirmed to have bi-functional effect when they are attached to the Pt catalyst for methanol oxidation reaction ^(3, 32). Furthermore, high cost Ru **can be eliminated**, the potential problems of Ru dissolution and crossover effect can be avoided.

In this study, we have designed a Pt deposited on novel nanosize Nb doped TiO₂ half-sphere shell (HSS) catalyst, which has significantly improved the methanol oxidation activity through three **combined** effect. As the conductivity of TiO₂ nanomaterial is not high enough to be applied as the catalyst substrates, the Nb dopant is used to improve their conductivity by creating oxygen vacancies ^(33, 34). The HSS Nb doped TiO₂ (named as Nb-TiO₂-HSS) substrate was further modified with Pt nanoparticles using a polyol method, thus forming the final catalyst named as Pt/Nb-TiO₂-HSS. Compared to the conventional catalyst such as PtRu/C, there are many advantages using this specially designed substrate material: (1) It improves mass transport during methanol oxidation by altering the diffusion mechanism of the fuel when the catalysts are embedded with the carbon gas diffusion layer (GDL). (2) The **metal oxide substrate facilitates methanol oxidation through strong metal support interactions (SMSI), and the intimate contact with Pt nanoparticles will provide hydroxyls group for =CO oxidation**. (3) The HSS nanostructure improves the durability of the catalyst by minimising the Pt dissolution, thus the DMFC prepared with Pt/Nb-TiO₂-HSS should have extended durability compared to commercial PtRu/C catalyst.

2. Experimental

2.1 Catalyst Preparation

All reagents are purchased from Sigma–Aldrich, U.K. The preparation procedure of the Pt/Nb-TiO₂-HSS electrocatalyst and its corresponding transmission electron microscopy (TEM) images of the fabricated nanostructures after each step are illustrated in **Fig. 1**. Briefly, SiO₂ spherical powders as template were synthesized using the hydrolysis of tetraethyl orthosilicate (TEOS) (**Fig. 1(a)**). Then the Nb-TiO₂ gel with 10% Nb (from sol-gel method) was coated on the surfaces of SiO₂ spheres using hydrolysis of tetrabutyl titanate (TBOT) followed by drying in an oven at temperature of 200 °C in air (Step 1). The obtained Nb-TiO₂@SiO₂ powder was annealed at 500 °C (**Fig. 1(b)**), and then were etched in NaOH at 70 °C for 6 hours (Step 2). The subsequent NaOH etching treatment resulted in the morphological transition from the Nb-TiO₂@SiO₂ core-shell into the well-defined Nb-TiO₂ shell nanocrystal by completely removing the inner SiO₂ core. As for the Nb-TiO₂, half of its shell was removed during the NaOH etching through carefully controlled reaction condition. Consequently, a distinctly circular opening of each Nb-TiO₂ HSS appeared, see **Fig. 1(c)**. The last step was the deposition of 5 wt% Pt nanoparticles onto Nb-TiO₂-HSS using a polyol method (step 3 in **Fig. 1**). Nb-TiO₂-HSS was mixed with ethylene glycol and deionized water, appropriate amount of H₂PtCl₆·6H₂O was added into mixture drop wisely, and then the *pH* value of the solution was adjusted to 11 by adding 1 M NaOH. The reaction was carried out for 4 hours under N₂ atmosphere at 120 °C, and then cooled down to room temperature followed by mixing for another 12 hours. The product was washed, separated then dried overnight in open air oven. The obtained catalyst is name as Pt/Nb-TiO₂-HSS and shown in **Fig. 1(d)**. **More details of the catalyst preparation can be found in Supporting Information (SI).**

2.2 Materials Characterisation

Surface morphology was analysed using a scanning electron microscope (SEM/JEM-2100F) attached with an EDX analyser and TEM images were obtained using a FEI Tecnai G2 F20 at 100 kV. XRD patterns were recorded using a Bruker D8 Focus machine operated at 40 kV and 40 mA equipped with a nickel-filtered Cu K α radiation ($\lambda = 1.54056 \text{ \AA}$) and a 2θ ranging from 10 to 90° at a scanning rate of 0.02° per step and 0.15 second per step. Phase identification was carried out using X'Pert High Score software associated with the ICDD database PDF2-2004. X-ray photoelectron spectroscopy (XPS, Kratos Axis Nova spectrometer) was used to analyse the composition and interaction of each element in the catalysts, the data were analysed using CasaXPS. Brunauer-Emmett-Teller (BET) surface area and pore structure of the catalysts were measured using a Micromeritics Tristar3000 analyser by nitrogen adsorption at 77 K before the deposition of Pt nanoparticles. Elemental analysis of catalysts was also performed using an ICP-OES (Varian Vista-MPX) at a high frequency emission power of 1.5 kW and a plasma airflow of 15.0 L/min ($\lambda_{Pt} = 214.424 \text{ nm}$, $\lambda_{Si} = 251.611 \text{ nm}$, $\lambda_{Ce} = 418.659 \text{ nm}$)

2.3 Electrochemical Evaluation

Electrochemical evaluation experiments were carried out using an AutoLab PGSTAT30 potentiostat/galvanostat. Cyclic voltammetry (CV), CO stripping and methanol oxidation linear voltammetry were to study the catalytic activity of the catalysts. Half-cell electrochemical tests were conducted using a BASi RRDE-3A package which consists of a glassy carbon (GC) rotating disk electrode (RDE) with a surface area of 0.1256 cm², a glass cell vial (100 ml), an Ag/AgCl reference electrode, a 7.5 cm long Pt wire with 0.5 mm diameter. The potentials obtained in this study were referred to the reference hydrogen electrode (RHE). The loading of catalyst deposited

on the GC disk was 0.5 mg cm^{-2} . The ink was prepared by ultrasonically mixing the catalysts and 5.0 wt% Nafion ionomer in ethanol. A required amount of the catalyst slurry was carefully dropped on glassy carbon surface and allowed to dry at room temperature for 15 minutes to obtain a uniform catalyst film. CVs were recorded in 0.5 M H_2SO_4 solution. All half-cell experiment was carried out at room temperature. For the CO stripping experiment, the catalysts were sprayed on Toray TGHP-90 carbon paper with a Pt loading of 0.5 mg cm^{-2} , and round shape buttons with 0.785 cm^2 were cut off to act as the working electrodes. The test was carried out in the same half-cell apparatus with the electrolyte being 0.5 M H_2SO_4 , and the working electrodes were climbed using a thin gold wire. CO gas was used to purge through the electrolyte for 20 minutes followed by 10 minutes purging with N_2 to remove any residuals CO in the electrolyte. The electrodes were scanned three times between 0 V to 1.1 V vs. RHE. The methanol oxidation linear voltammetry were performed using the same RDE and CV tests at a rotating rate of 900 rpm and a scan rate of 5 mV s^{-1} at room temperature for Pt/Nb-TiO₂-HSS catalyst, PtRu/C and Pt/C, respectively, the electrolyte was 1 M methanol in 0.5 M H_2SO_4 .

In the miniature direct methanol fuel cell test, same catalysts and Nafion solution were used, the ink prepared with requested amount of catalysts, then sprayed evenly onto Toray TGHP-90 carbon paper and dried at 85 °C on a hot plate. The metal loading of Pt or PtRu were 1.5 mg cm^{-2} . The electrodes have an area of 3.14 cm^2 , the membrane used here is Nafion 117[®], the MEA was hot pressed at 110 °C then cooled down to room temperature.

3. Results and Discussions

Fig. 2a shows the scanning electron microscopy (SEM) image of the Nb-TiO₂ nanostructures, which have a uniform-sized HSS with an average diameter of $148 \pm 10 \text{ nm}$. After deposited with

the Pt nanoparticles, the resulted Pt/Nb-TiO₂-HSS catalyst (**Fig. S1a**) shows the similar morphology as those of Nb-TiO₂-HSS. **Figs. 2b** and **2c** show the detailed nanostructures of Nb-TiO₂-HSS and Pt/Nb-TiO₂-HSS obtained from TEM. The average diameter of the Nb-TiO₂-HSS nanostructure was further confirmed by **Fig. 2b** (~148nm) and shows an opening on its surface. From **Fig. 2c**, the average diameter of the Pt particles is about 10±1 nm and these particles are homogeneously dispersed on (mostly inside the half shell) the substrate.

The crystallinity of the obtained nanostructures was characterized using X-ray diffraction (XRD) and the results are shown in **Fig. 3**. It can be clearly observed the diffraction peaks for Nb-TiO₂-HSS belongs to anatase TiO₂. Interestingly, there is no apparent XRD peak corresponding to Nb. That is because the Ti atoms in the TiO₂ lattice structures can be substitutionally replaced by Nb atoms. As the ionic radii of Nb atoms are smaller than those of Ti, thus when the Ti atoms are replaced by Nb atoms, the lattice will become shrinkage, which could limit the growth of crystallite. Similar phenomena have been observed in other Nb doped TiO₂ nano particles works⁽³⁵⁾. And due to the Nb atoms doping, the diffraction peaks of TiO₂ are shifted to small angles. While after loading the Pt nanoparticles, the resulted Pt/Nb-TiO₂-HSS sample also shows strong Pt peaks, corresponding to the (111), (200), (220) lattice plane⁽³⁶⁾. And due to extremely strong diffraction peaks of Pt, which greatly affect some weak characteristic diffraction peaks of TiO₂, resulting some of the diffraction peaks of TiO₂ disappeared in the spectrum of Pt/Nb-TiO₂-HSS. Similar phenomena have been observed in other Nb doped TiO₂ nano particles works⁽³⁵⁾.

The existence of Nb can be confirmed through analysis using energy dispersive X-ray analysis (EDX) and inductively coupled plasma-optical emission spectrometry (ICP-OES). In the EDX spectrum of the Pt/Nb-TiO₂-HSS is shown in **Fig. S1b** with signals of Ti, O, Nb, Pt. No Si peak can be detected from the EDX spectrum, indicating that the SiO₂ was removed completely after

etching process. EDX elemental analysis shows that the nanostructures have 9.80 wt% of Nb and 5.24 wt% of Pt. Precisely elemental analysis of nanostructures using the ICP-OES (Varian Vista-MPX) operated at a high frequency emission power of 1.5 kW and a plasma airflow of 15.0 L/min ($\lambda_{Pt}=214.424$ nm, $\lambda_{Si} = 251.611$ nm, $\lambda_{Ce} = 418.659$ nm) show that Nb is 9.41 wt% and Pt is 5.12 wt%.

XPS was used to analyse the composition and interaction of each element in the catalysts. The resulting peak positions were corrected according to the peak of carbon. As shown in **Fig. 4a**, the survey spectrum of Pt/Nb-TiO₂-HSS catalyst demonstrate the existence of Nb, Ti, Pt and O. To analyse the interactions between Nb and the TiO₂ matrix, as well as the influence from the substrate to Pt nanoparticles, Ti *2p*, Nb *3d* and Pt *4f* spectra were collected and shown in **Fig. 4b, 4c and 4d**, respectively. The XPS spectra of Ti *2p* electrons showed the dominant peaks are at 458.1 eV and 464.2 eV, resulted from Ti(IV). They had 4.6 eV and 3.7 eV shift to lower binding energies (BEs) from 453.5 eV and 460.5 eV of Ti(IV). **Nb dopant with up to 25% weight content would not change Ti's BEs for nanoparticles** ⁽³⁷⁾, however, morphology change will influence the BEs for Nb doped TiO₂ nanostructures, e.g. Kim et al. reported Nb doped TiO₂ nanowire has Ti*2p* BEs at 459.3 and 465.0 eV ⁽³⁸⁾. Our catalyst shows an even further negative shift, which is highly likely caused by the special HSS structure. Another reason for such big shift is the introduction of Nb dopant altered the electronic structure of Ti-O-Ti, this agrees to several other researchers work in this field ^(20, 39-41), as well as the existence of hydroxyl group which also plays a role of changing the BEs ^(42, 43). The XPS spectra of Nb *3d* electrons indicated dominant peaks at 207.4 eV and 210.0 eV resulted from Nb(V). These BEs agreed with those of Nb₂O₅ particles as well as Nb doped TiO₂ particles ^(39, 44, 45), **which indicate that Nb *3d* BE was not affected by the TiO₂ matrix and HSS structure.** The other peaks with lower intensities are attributed to Nb(II) and Nb(IV) species ^(46, 47). **Fig. 4d**

shows the Pt *4f* XPS spectra. The most intense peaks, observed at 67.3 eV and 71.7 eV were attributed to zero-valent platinum. These BEs were lower than for pure Pt particles, due to the interaction of the support material^(14, 41). It has been intensively discussed that the SMSI effects on the nano-catalysts' electronic structure and therefore the catalytic activity⁽⁴⁸⁻⁵⁰⁾. SMSI can be interpreted as partial charge transfer^(51, 52) or substrate-induced change in the lattice parameter of the metal deposited⁽⁵³⁾. Unlike porous carbon substrate materials, TiO₂ act as a donor of electrons, doping Nb will create more oxygen vacancies which further facilitates electron transfer. Such electronic structure changes can be reflected as the shifts of Pt *4f* and Ti *2p* XPS signals toward lower BEs. It can be noticed that there are further 3.1 eV and 2.2 eV shift lower than that of Nb doped TiO₂ ordinary shaped nanoparticle supported Pt catalysts^(3, 54). These are the strong evidence that the special HSS structure affects the BEs. The second set of peaks, with BEs of about 68.4 eV and 75.4 eV, were assigned to the Pt(II) state in PtO and Pt(OH)₂-like species^(47, 55, 56). Again, these peaks are shifted towards lower BEs comparing to pure Pt, carbon supported Pt and TiO₂ supported Pt, and a further shift to lower BEs is also observed while comparing to ordinary Nb doped TiO₂ supported Pt catalyst which has good agreement with effect to zero-valent Pt. The XPS elementary composition analysis results also confirmed the Pt content is 5.03 wt%.

To confirm that the Nb-TiO₂-HSS is suitable to be used as catalyst substrate materials. We used a Brunauer-Emmett-Teller (BET) method to measure the surface areas of the Nb-TiO₂-HSS substrate nanostructures, and obtained an average value of ~217 m² g⁻¹. This is comparable to the high value obtained from a commercially used surface carbon black substrate (~250 m² g⁻¹). Such a large BET surface area is beneficial for catalytically chemical processes and also for depositing the Pt nanoparticles in order to achieve a high catalytic activity.

To demonstrate the catalytic activity of the Pt/Nb-TiO₂-HSS catalyst, we evaluated the catalyst using various electrochemical methods. Commercially available Pt/C (HiSPEC4000) and PtRu/C (HiSPEC10000) were also employed as the reference catalysts for comparison purposes. **Fig. 5a** shows the cyclic voltammograms (CV) of the Pt/Nb-TiO₂-HSS catalyst and Pt/C catalyst. The results obtained using our newly developed catalyst showed clear Pt features at the hydrogen under potential (UPD) region and higher charge on Pt oxidation for the commercial Pt/C catalyst. The Pt-O_x reduction peaks can be observed at the potentials between 0.5 V and 1.0 V vs. RHE on the reverse scan. Results clearly prove that the addition of Nb and the specially designed HSS morphology have dramatically increased the electrical conductivity of TiO₂.

CO stripping (**Fig. 5b**) and methanol oxidation reaction (MOR) linear scan tests (**Fig. 5c**) were used to further probe the nature of the catalyst by studying the SMSI, bi-functional mechanism and the catalytic activity of the catalyst. In the CO stripping test, the catalyst was scanned three times between 0 V to 1.1 V vs. RHE after CO poisoning. The results from the first and third scans are shown in **Fig. 5b**. It is clear that the CO oxidation onset potential of the Pt/Nb-TiO₂-HSS catalyst is 0.28 V vs. RHE, which is much lower than 0.70 V vs. RHE of the Pt/C catalyst. This clearly shows the evidence of the bifunctional effect generated from the Nb doped TiO₂ HSS substrate material. The CO stripping electrochemical surface area per Pt (ECSA) is calculated using equation (1):

$$\text{ECSA (m}^2 \text{ g}^{-1} \text{ Pt)} = \text{Charge} / \text{Pt loading} \times 0.42 \quad (1)$$

Where, Charge represents the charge (C) for CO stripping area obtained from AutoLab electrochemical workstation, Pt loading represents the platinum loading in the electrode and 0.42 represents the charge required to oxidise a monolayer of CO on the Pt surface. The ECSA of Pt/Nb-TiO₂-HSS is measured as 22.1 m² g⁻¹ Pt, this is comparable to PtRu/C commercial catalyst with

ECSA of $22.8 \text{ m}^2 \text{ g}^{-1} \text{ Pt}$, however, it has to be noted that HiSPEC10000 catalyst's average particle size is around 4 nm, this will dramatically improve the active surface area of noble metal (Pt and Ru), Ru is preoccupied with -OH during the process of CO poisoning, so the surface area of Ru did not contribute to ESCA using CO stripping method, this is well agreed with many other researchers' work ⁽⁵⁷⁻⁵⁹⁾. Commercial Pt/C catalyst HiSPEC4000 shows a ECSA of $60 \text{ m}^2 \text{ g}^{-1} \text{ Pt}$ which is nearly 3 times higher than our catalyst, this can be easily understand from the particle size effect ⁽⁶⁰⁾. The MOR test results are shown in **Fig. 5c**, both Pt/Nb-TiO₂-HSS and PtRu/C catalysts have significant lower onset methanol oxidation potential than that of the Pt/C. The onset potential of Pt/Nb-TiO₂-HSS is 0.21 V vs. RHE, which is 0.05 V lower than 0.26 V vs. RHE of PtRu/C. This could be attributed to the SMSI effect which has been well discussed in XPS results analysis. The increased methanol oxidation activity is mainly attributed to the consequence of the existing surface bridging hydroxyls which are bonded spontaneously onto the HSS surface once it is exposed to any forms of water ^(42, 43, 61). In addition, the improved activity is also benefited from the Nb-TiO₂-HSS nanostructures and the water bonding property of Nb-TiO₂, which have been previously explained by Pan *et al.* ⁽²³⁾. The surface bridging hydroxyls existing on the TiO₂ surfaces can retain certain amount of water molecules, and thus the adjacent water can form new bridging hydroxyls once the 'old' ones are reacted with =CO ⁽²²⁾. Moreover, these unique HSS structures dramatically increase the surface areas of the catalyst. They will also alter the arrangement of =CO and -OH, compared with that in the conventional PtRu/C catalysts. The increased -OH amounts of molecules improve the methanol oxidation rate so that theoretically the reaction rate and mass transport will be improved. The formation of hydroxyls releases H⁺ which will increase the ζ potential, and thus lead to a decrease of pH value. Meanwhile, the addition of

Nb leads to the formation of more electronic vacancies ⁽²¹⁾, which will then increase the conductivity of the catalyst.

The Pt/Nb-TiO₂-HSS catalyst and commercial PtRu/C were both tested as anode materials in a miniaturized direct methanol fuel cell. Anode polarisation was operated at temperatures of 60 and 80 °C. The cell was operated in a driven cell mode, in which the cathode was fed with dry hydrogen acting as a reference and counter electrode, and 2 M methanol was passed through the anode. In this way, the potentiostatic test applied a constant potential to the electrode. The generated current was measured, so that the sample was protected from the high potential spikes which could dissolve the metal in the sample. The potentiostatic curves were obtained in the potential range from 0.025 V to 0.6 V *vs.* RHE using a step potential of 25 mV, and a holding time of 10 seconds per reading. The results are shown in **Fig. 5d**. At both testing temperatures, the Pt/Nb-TiO₂-HSS catalyst has slightly lower methanol oxidation onset potentials gives lower overpotential, as a consequence a better performance compared with those of the commercial PtRu/C catalyst.

Methanol oxidation (stripping) experiments are also performed to assess the intrinsic catalytic activity of the catalyst and to reveal the Pt electrochemical surface area. 2M methanol was flushed through the anode for 10 minutes then washed with Di-ionized water for 1 hour to remove any residual methanol retained within the electrode. Similar to CO stripping test, the electrode was scanned between 0 V to 0.8 V *vs.* RHE at scan rate of 5 mV s⁻¹ at 60 °C. The results of methanol stripping are shown in **Fig. S2**, and the ECSA per Pt was calculated using equation (1), because Pt=CO forms on the surface of Pt nanoparticles during methanol ‘poisoning’ process. Commercial PtRu/C had an ECSA of 25.6 m² g⁻¹ Pt which is generally agreed with CO stripping result. However, Pt/Nb-TiO₂-HSS showed an ECSA of 26.9 m² g⁻¹ Pt which is higher than CO stripping result, such improvement could attribute to the better utilisation of Pt of the new catalyst, or the elevated

temperature. Another assumption is that 1-hour washing was not able to remove all residual methanol retained within the HSS structure, and the remaining methanol contributed to the methanol oxidation charge.

Cathode polarisation test was then conducted using the same minicell configuration at 80 °C, pure O₂ was fed into the cathode with a flow rate of 200 cm³ min⁻¹. The flow rate of 2 M methanol for the anode was 2 cm³ min⁻¹. The scan rate was 5 mV s⁻¹. The cathode catalyst was 50%wt Pt/C with loading of 1.5 mg cm⁻² on the electrode. The obtained polarization and power curves are shown in **Fig. 5e**. Unlike those in the anode polarisation results, the Pt/Nb-TiO₂-HSS catalyst has a maximum power output of 0.0931 W which is slightly lower than 0.0952 W of the PtRu/C, but both of which are significantly higher than the one of 0.050 W achieved from the commercial Pt/C. Both anode and cathode polarisation results clearly provide the evidence of the SMSI and bifunctional effect of the TiO₂-Nb-HSS substrate material, which show that the Pt/Nb-TiO₂-HSS has a competitive methanol oxidation activity and good DMFC performance compared with the commercial PtRu/C catalyst. The observation also suggests an improvement in mass transport during methanol oxidation reaction, as the special HSS structure could alter the diffusion of liquid fuel, and a micro-scale laminate flow can be assumed while 2 M methanol passes those HSSs.

Durability tests using both the Pt/TiO₂-Nb-HSS and PtRu/C catalysts were also performed using the same experimental conditions of the cathode polarisation tests for 200 scans at 80 °C (**Fig. 5f**), new 2 M methanol was changed every 10 cycles to keep a steady concentration. Results clearly show that there is almost no apparent decrease in the maximum power from the Pt/Nb-TiO₂-HSS catalyst, whereas the PtRu/C catalyst has a nearly 10% drop after 200 scans. The improved durability can be explained by the minimization of the catalyst dissolution and the formation of specially designed HSS nanostructures which prevent Pt loss during the catalytic

reactions.

4. Conclusions

In summary, Pt/Nb-TiO₂-HSS catalyst has been successfully designed and synthesized with well-defined, uniform HSS shapes. The conductivity of such material has been improved by doping with Nb, which is suitable as catalyst's substrate material. The average diameter of the Pt particles is estimated to be $\sim 10 \pm 1$ nm and well-dispersed within Nb-TiO₂-HSS. Half-cell electrochemical evaluation revealed that the Pt/Nb-TiO₂-HSS catalyst has clear **SMSI effect, bi-functional** effect and a comparable catalytic activity compared to the commercially used PtRu/C catalyst. Good performance for the methanol oxidation activity using the catalyst have been verified from the miniature fuel cell tests. The improved mass transport and durability of Pt/Nb-TiO₂-HSS catalyst is attributed to the minimization of the catalyst dissolution and the formation of specially designed HSS structures which prevent Pt loss during the catalytic reactions. The unique nanostructure and synthesis method could offer a new strategy for synthesis of many other types of advanced metal oxide-based micro-/nano-materials. More importantly, this newly developed Pt modified Nb-TiO₂ HSS catalysts can be easily synthesized in a large process scale, revealing a promising feature for the commercialisation of DMFCs.

Acknowledgement

We would like to acknowledge the Engineering and Physical Sciences Research Council (EPSRC) grant number: EP/S032886/1 and Chongqing Research Program of Basic Research and Frontier Technology, grant numbers cstc2016jcyjA0142 and cstc2017jcyjAX0236 for funding support.

Reference

1. N. Kakati, J. Maiti, S. H. Lee, S. H. Jee, B. Viswanathan and Y. S. Yoon, *Chem. Rev.*, **114**, 12397 (2014).
2. E. H. Yu*, X. Wang, X. T. Liu and L. Li, in *Catalysts for Alcohol-Fuelled Direct Oxidation Fuel Cells*, p. 227, The Royal Society of Chemistry (2012).
3. X. Liu, X. Wu and K. Scott, *Catalysis Science & Technology*, **4**, 3891 (2014).
4. X. Liu, J. Xi, B. B. Xu, B. Fang, Y. Wang, M. Bayati, K. Scott and C. Gao, *Small Methods*, **2**, 1800138 (2018).
5. T. Iwasita, *Electrochimica Acta*, **47**, 3663 (2002).
6. J. Y. Damte, S.-I. Lyu, E. G. Leggesse and J. C. Jiang, *Physical Chemistry Chemical Physics*, **20**, 9355 (2018).
7. S. Lu, H. Li, J. Sun and Z. Zhuang, *Nano Research*, **11**, 2058 (2018).
8. X. Jing, G. Sheng, H. Fei, L. Jing and Z. Lianming, *International Journal of Quantum Chemistry*, **118**, e25491 (2018).
9. F. Yang, B. Zhang, S. Dong, Y. Tang, L. Hou, Z. Chen, Z. Li, W. Yang, C. Xu, M. Wang, Y. Li and Y. Li, *Applied Surface Science*, **452**, 11 (2018).
10. R. S. Amin, R. M. Abdel Hameed, K. M. El-Khatib and M. Elsayed Youssef, *International Journal of Hydrogen Energy*, **39**, 2026 (2014).
11. K.-W. Park, J.-H. Choi, B.-K. Kwon, S.-A. Lee, Y.-E. Sung, H.-Y. Ha, S.-A. Hong, H. Kim and A. Wieckowski, *The Journal of Physical Chemistry B*, **106**, 1869 (2002).
12. E. Antolini, J. R. C. Salgado and E. R. Gonzalez, *Applied Catalysis B: Environmental*, **63**, 137 (2006).
13. E. N. El Sawy and V. I. Birss, *ACS Applied Materials & Interfaces*, **10**, 3459 (2018).
14. X. Liu, E. H. Yu and K. Scott, *Applied Catalysis B: Environmental*, **162**, 593 (2015).
15. K. Taehyun, J. Minki, K. H. Young, O. Aram, P. Jongsik, B. Hionsuck, J. S. Hoon and L. Kwangyeol, *Advanced Functional Materials*, **28**, 1706440 (2018).
16. M. Bayati, X. Liu, P. Abellan, D. Pocock, M. Dixon and K. Scott, *ACS Applied Energy Materials*, **3**, 843 (2020).
17. E. Antolini, *Journal of Solid State Electrochemistry*, **15**, 455 (2011).
18. Y. Xinxin, X. Zejun, Y. Zehui, X. Sen, Z. Quan, L. Ying, Z. Yunfeng and C. Weiwei, *Nanotechnology*, **29**, 245401 (2018).
19. J. Wen, X. Li, W. Liu, Y. Fang, J. Xie and Y. Xu, *Chinese Journal of Catalysis*, **36**, 2049 (2015).
20. J. Lu, P. Zhang, A. Li, F. Su, T. Wang, Y. Liu and J. Gong, *Chemical Communications*, **49**, 5817 (2013).
21. T. Nikolay, L. Larina, O. Shevaleevskiy and B. T. Ahn, *Energy & Environmental Science*, **4**, 1480 (2011).
22. E. Jiang, X. Liu, H. Che, C. Liu, H. Dong and G. Che, *RSC Advances*, **8**, 37200 (2018).
23. J. H. Pan, X. Zhang, A. J. Du, D. D. Sun and J. O. Leckie, *Journal of the American Chemical Society*, **130**, 11256 (2008).
24. L. Pan, J.-J. Zou, X. Zhang and L. Wang, *Journal of the American Chemical Society*, **133**, 10000 (2011).
25. J. Lu, L. Lan, X. T. Liu, N. Wang and X. Fan, *Frontiers of Chemical Science and Engineering*, **13**, 665 (2019).

26. D. Zhang, B. Wang, Y. Jiang, P. Zhou, Z. Chen, B. Xu and M. Yan, *Journal of Alloys and Compounds*, **653**, 604 (2015).
27. Z. Li, H. Li, Z. Wu, M. Wang, J.-t. Luo, H. Torun, P. Hu, C. Yang, M. Grundmann, X. Liu and Y. Q. Fu, *Materials Horizons* (2018).
28. Z. Li, H. Li, Z. Wu, M. Wang, J. Luo, H. Torun, P. Hu, C. Yang, M. Grundmann, X. Liu and Y. Fu, *Materials Horizons*, **6**, 470 (2019).
29. N. R. Elezović, B. M. Babić, L. Gajić-Krstajić, V. Radmilović, N. V. Krstajić and L. J. Vračar, *Journal of Power Sources*, **195**, 3961 (2010).
30. L. Zhang, X. Ji, X. Wang, Y. Fu, H. Zhu and T. X. Liu, *Journal of The Electrochemical Society*, **167**, 024507 (2020).
31. K. Fujishima and A. Honda, *Nature* **238**, 37 (1972).
32. G. Liu, H. Zhang, J. Hu, Y. Zhai, D. Xu and Z.-g. Shao, *Journal of Power Sources*, **162**, 547 (2006).
33. M. Kato, H. Najima and T. Ozawa, *Journal of The Electrochemical Society*, **166**, H468 (2019).
34. D. Regonini, A. Groff, G. D. Sorarù and F. J. Clemens, *Journal of The Electrochemical Society*, **163**, H243 (2016).
35. J. Zhu, Z. Deng, F. Chen, J. Zhang, H. Chen, M. Anpo, J. Huang and L. Zhang, *Applied Catalysis B: Environmental*, **62**, 329 (2006).
36. P. Bera, K. R. Priolkar, A. Gayen, P. R. Sarode, M. S. Hegde, S. Emura, R. Kumashiro, V. Jayaram and G. N. Subbanna, *Chemistry of Materials*, **15**, 2049 (2003).
37. B. K. Kaleji, R. Sarraf-Mamoory and A. Fujishima, *Materials Chemistry and Physics*, **132**, 210 (2012).
38. M. Kim, C. Kwon, K. Eom, J. Kim and E. Cho, *Scientific Reports*, **7**, 44411 (2017).
39. T. Ruff, R. Hahn, M. S. Killian, H. Asoh, S. Ono and P. Schmuki, *Electrochimica Acta*, **62**, 402 (2012).
40. Y. Zeng, W. Wu, S. Lee and J. Gao, *Catalysis Communications*, **8**, 906 (2007).
41. S. Hussain, N. Kongi, H. Erikson, M. Rähn, M. Merisalu, L. Matisen, P. Paiste, J. Aruväli, V. Sammelselg, L. A. Estudillo-Wong, K. Tammeveski and N. Alonso-Vante, *Electrochimica Acta*, **316**, 162 (2019).
42. L. Nie, J. Yu, X. Li, B. Cheng, G. Liu and M. Jaroniec, *Environmental Science & Technology*, **47**, 2777 (2013).
43. L. Kong, C. Wang, F. Wan, L. Li, X. Zhang and Y. Liu, *Dalton Transactions*, **46**, 15363 (2017).
44. F. Verpoort, G. De Doncker, A. R. Bossuyt, L. Fiermans and L. Verdonck, *Journal of Electron Spectroscopy and Related Phenomena*, **73**, 271 (1995).
45. L. Kong, X. Liu, J. Wei, S. Wang, B. B. Xu, D. Long and F. Chen, *Nanoscale*, **10**, 14165 (2018).
46. O. Friedrichs, J. C. Sánchez-López, C. López-Cartes, T. Klassen, R. Bormann and A. Fernández, *The Journal of Physical Chemistry B*, **110**, 7845 (2006).
47. S. Martínez-Méndez, Y. Henríquez, O. Domínguez, L. D'Ornelas and H. Krentzien, *Journal of Molecular Catalysis A: Chemical*, **252**, 226 (2006).
48. A. Lewera, L. Timperman, A. Roguska and N. Alonso-Vante, *The Journal of Physical Chemistry C*, **115**, 20153 (2011).
49. S. J. Yoo, T.-Y. Jeon, K.-S. Lee, K.-W. Park and Y.-E. Sung, *Chemical Communications*, **46**, 794 (2010).

50. W. Vogel, L. Timperman and N. Alonso-Vante, *Applied Catalysis A: General*, **377**, 167 (2010).
51. J. A. Horsley, *Journal of the American Chemical Society*, **101**, 2870 (1979).
52. B. H. Chen and J. M. White, *The Journal of Physical Chemistry*, **86**, 3534 (1982).
53. L. Timperman, A. Lewera, W. Vogel and N. Alonso-Vante, *Electrochemistry Communications*, **12**, 1772 (2010).
54. X. Liu, K. Zhang, J. Lu, K. Luo, J. Gong, V. K. Puthiyapura and K. Scott, *ChemCatChem*, **7**, 1543 (2015).
55. Z. Liu, B. Guo, L. Hong and H. Jiang, *Journal of Photochemistry and Photobiology A: Chemistry*, **172**, 81 (2005).
56. H.-J. Chun, D. B. Kim, D.-H. Lim, W.-D. Lee and H.-I. Lee, *International Journal of Hydrogen Energy*, **35**, 6399 (2010).
57. J. Zhang, X. Qu, Y. Han, L. Shen, S. Yin, G. Li, Y. Jiang and S. Sun, *Applied Catalysis B: Environmental*, **263**, 118345 (2020).
58. J. H. Bae, J.-H. Park, M.-K. Seo and S. Kim, *Journal of Alloys and Compounds*, **822**, 153586 (2020).
59. P. Ochal, J. L. Gomez de la Fuente, M. Tsyppkin, F. Seland, S. Sunde, N. Muthuswamy, M. Rønning, D. Chen, S. Garcia, S. Alayoglu and B. Eichhorn, *Journal of Electroanalytical Chemistry*, **655**, 140 (2011).
60. M. Shao, J. H. Odell, S.-I. Choi and Y. Xia, *Electrochemistry Communications*, **31**, 46 (2013).
61. A. Papaderakis, O. Spyridou, N. Karanasios, A. Touni, A. Banti, N. Dimitrova, S. Armyanov, E. Valova, J. Georgieva and S. Sotiropoulos, *Catalysts*, **10**, 248 (2020).

Figure Captions

Fig. 1 Synthesis and formation process of Pt/Nb-TiO₂-HSS catalyst, TEM images reveal the morphological evolution

Fig. 2 TEM images of the as-prepared (a) SEM image of Nb-TiO₂, (b) Nb-TiO₂-HSS, and (c) Pt/Nb-TiO₂-HSS catalyst

Fig. 3 XRD patterns of Nb/TiO₂-HSS substrate and Pt/Nb-TiO₂-HSS catalyst.

Fig. 4 (a) XPS survey spectrum, (b) Ti 2*p*, (c) Nb 3*d* and Pt 4*f* XPS spectra of Pt/Nb-TiO₂-HSS catalyst

Fig. 5 Half-cell electrochemical evaluation results of (a) cyclic voltammograms of Pt/Nb-TiO₂-HSS and Pt/C and (b) CO stripping test curves of Pt/Nb-TiO₂-HSS, (c) methanol oxidation linear voltammograms of Pt/Nb-TiO₂-HSS, PtRu/C and Pt/C; as well as Miniature DMFC test results of (d) anode and (e) cathode polarisation curves and (f) durability test results of Pt/Nb-TiO₂-HSS and PtRu/C catalysts

Fig. 1

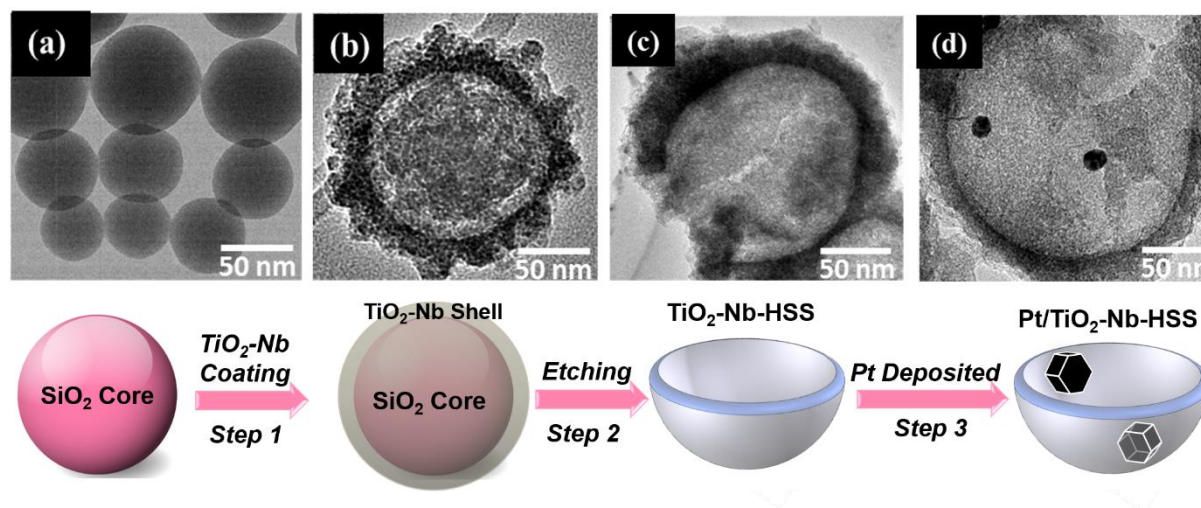


Fig. 2

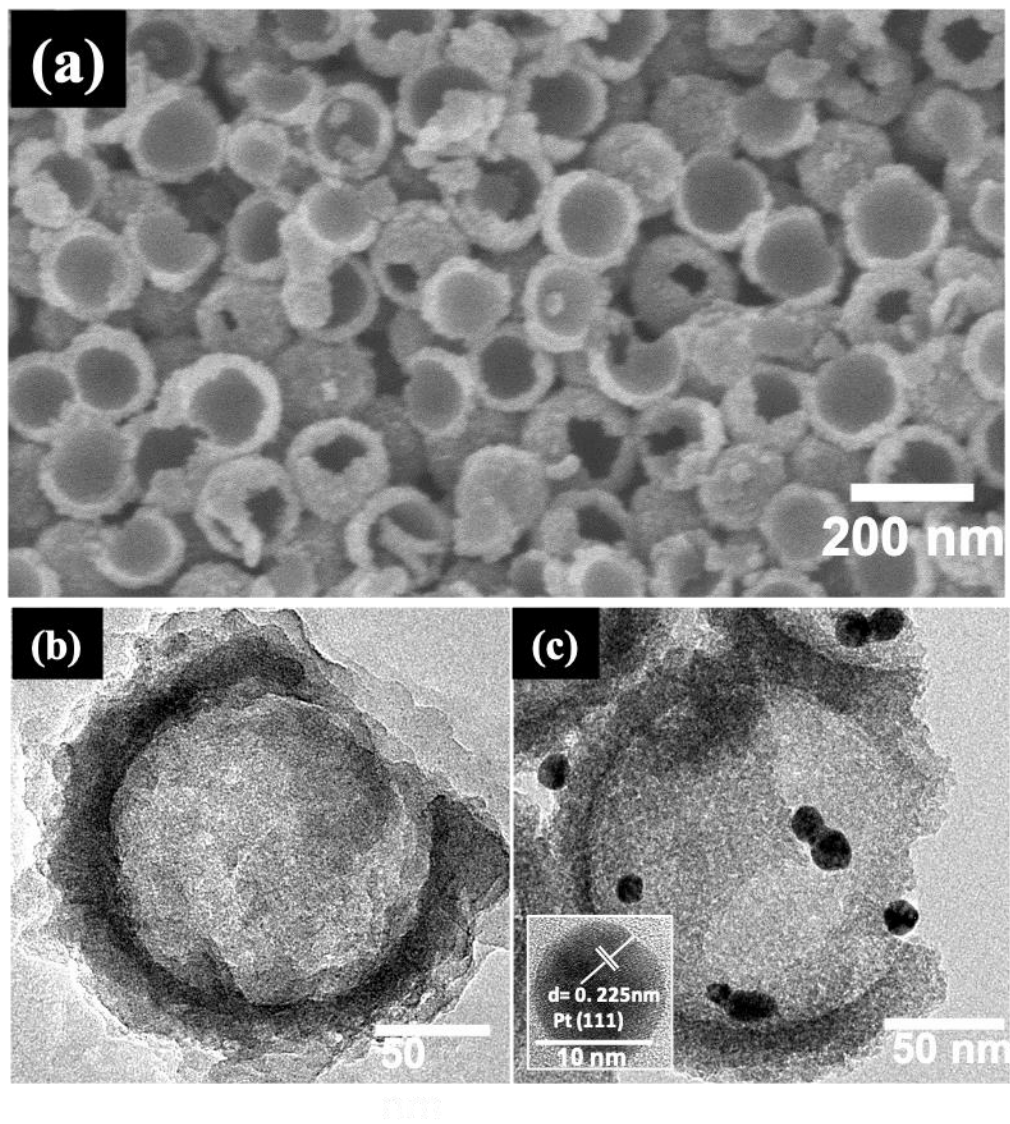


Fig. 3

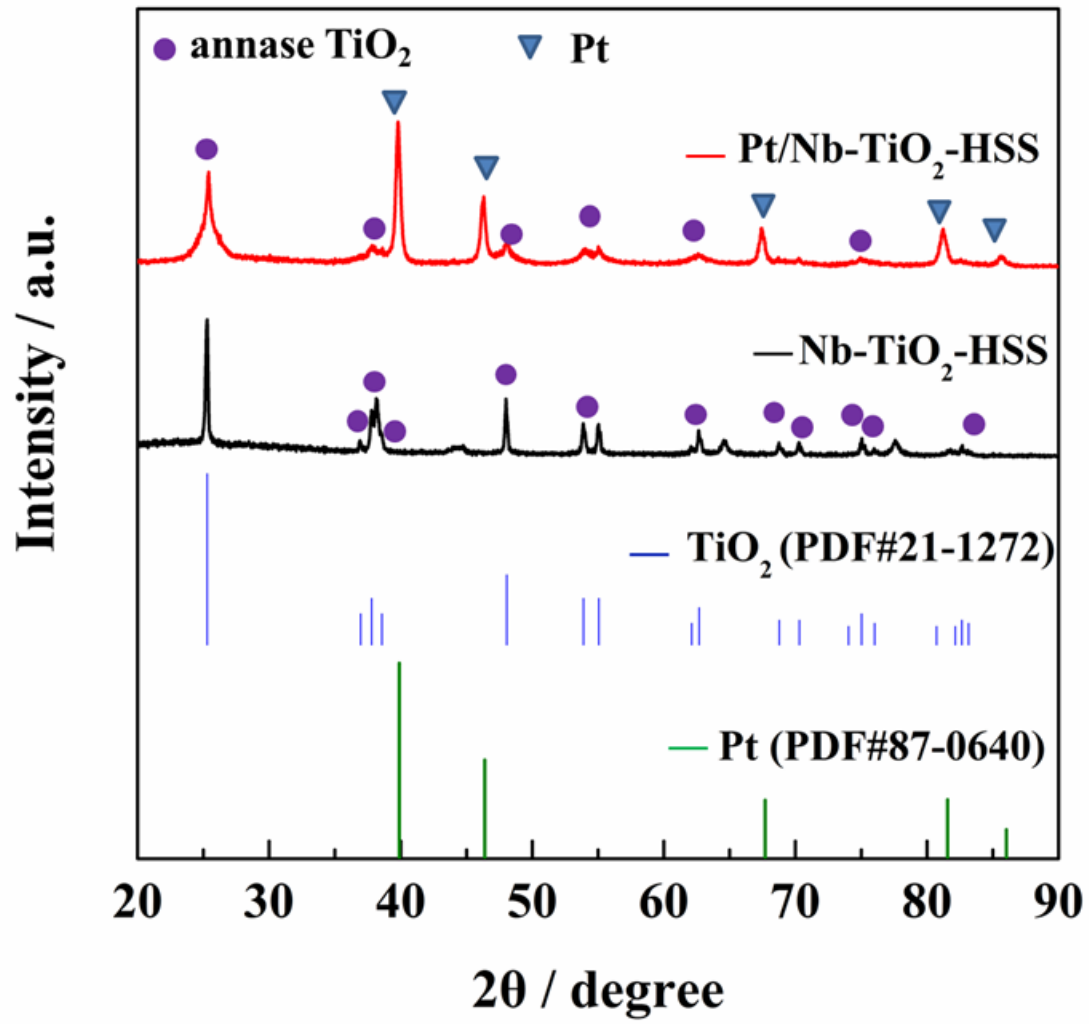


Fig. 4

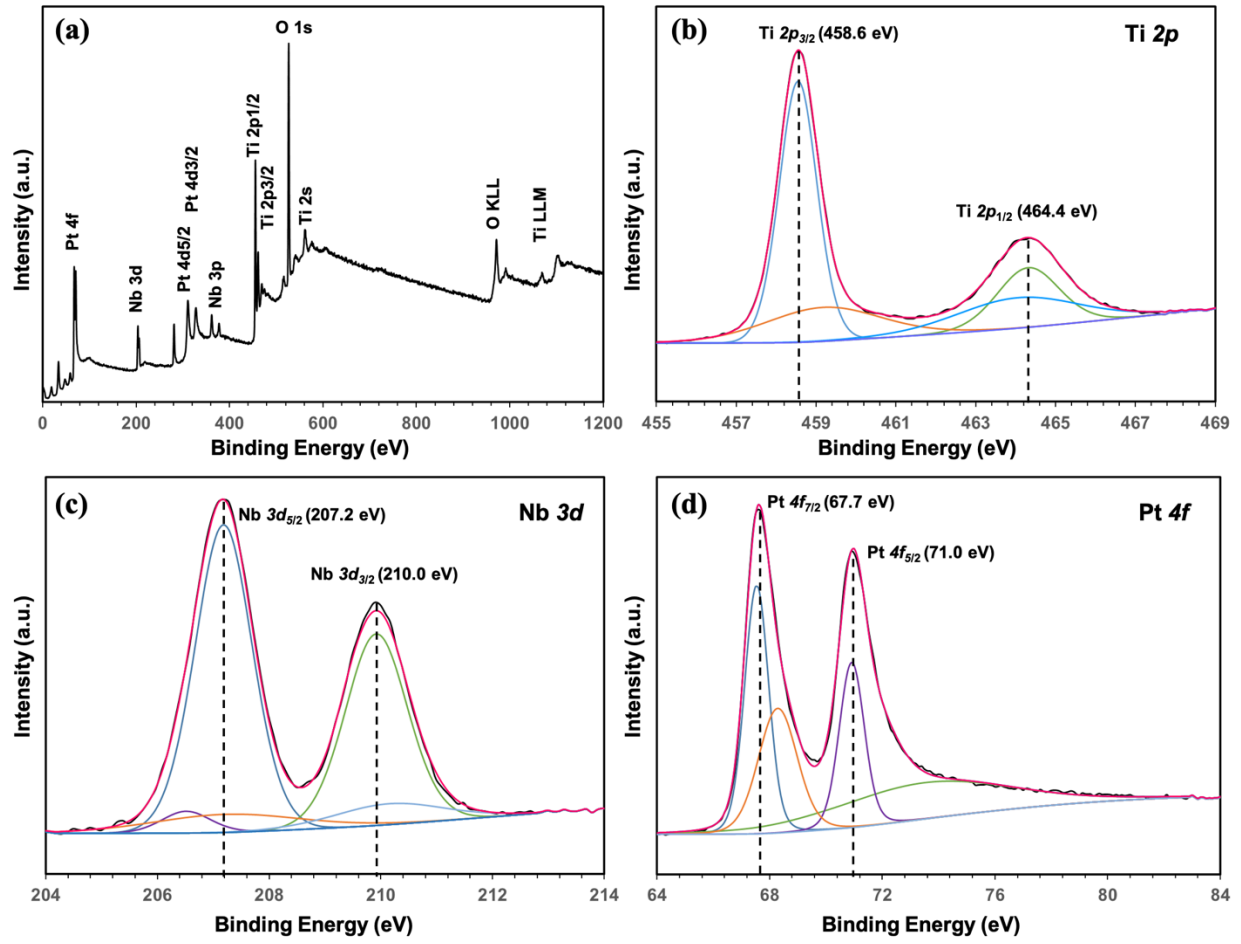


Fig. 5

